



JWST Observations of SN 2024ggi. II. NIRSpec Spectroscopy and CO Modeling at +285–385 Days past the Explosion

T. Mera¹ , C. Ashall² , P. Hoefflich¹ , K. Medler² , M. Shahbandeh³ , C. R. Burns⁴ , E. Baron^{5,6} , J. M. DerKacy³ , N. Morrell⁷, J. Lu⁸ , J. T. Hinkle^{2,9,10,19} , P. A. Mazzali^{11,12} , E. Fereidouni¹ , C. M. Pfeffer^{2,20} , S. Shiber¹ , T. Temim¹³ , L. Galbany^{14,15} , D. A. Coulter^{3,16} , L. Ferrari^{17,18} , W. B. Hoogendam^{2,20} , E. Y. Hsiao¹ , M. M. Phillips⁷ , and B. J. Shappee²

¹ Department of Physics, Florida State University, Tallahassee, FL 32306, USA

² Institute for Astronomy, University of Hawai'i at Manoa, 2680 Woodlawn Dr., Hawai'i, HI 96822, USA

³ Space Telescope Science Institute, 3700 San Martin Drive, Baltimore, MD 21218-2410, USA

⁴ Observatories of the Carnegie Institution for Science, 813 Santa Barbara St., Pasadena, CA 91101, USA

⁵ Planetary Science Institute, 1700 East Fort Lowell Road, Suite 106, Tucson, AZ 85719-2395, USA

⁶ Hamburger Sternwarte, Gojenbergsweg 112, 21029 Hamburg, Germany

⁷ Las Campanas Observatory, Carnegie Observatories, Casilla 601, La Serena, Chile

⁸ Department of Physics & Astronomy, Michigan State University, East Lansing, MI, USA

⁹ Department of Astronomy, University of Illinois Urbana-Champaign, 1002 West Green Street, Urbana, IL 61801, USA

¹⁰ NSF-Simons AI Institute for the Sky (SkAI), 172 E. Chestnut St., Chicago, IL 60611, USA

¹¹ Astrophysics Research Institute, Liverpool John Moores University, 146 Brownlow Hill, Liverpool L3 5RF, UK

¹² Max-Planck-Institut für Astrophysik, Karl-Schwarzschild Straße 1, 85748 Garching, Germany

¹³ Princeton University, 4 Ivy Lane, Princeton, NJ 08544, USA

¹⁴ Institute of Space Sciences (ICE, CSIC), Campus UAB, Carrer de Can Magrans, s/n, E-08193 Barcelona, Spain

¹⁵ Institut d'Estudis Espacials de Catalunya (IEEC), E-08034 Barcelona, Spain

¹⁶ Physics and Astronomy Department, Johns Hopkins University, Baltimore, MD 21218, USA

¹⁷ Instituto de Astrofísica de La Plata (IALP), CONICET, Paseo del Bosque S/N, B1900FWA La Plata, Argentina

¹⁸ Facultad de Ciencias Astronómicas y Geofísicas Universidad Nacional de La Plata, Paseo del Bosque, B1900FWA, La Plata, Argentina

Received 2025 October 20; revised 2025 December 5; accepted 2025 December 21; published 2026 January 30

Abstract

We present James Webb Space Telescope (JWST) Near-Infrared Spectrograph observations of SN 2024ggi, spanning wavelengths of 1.7–5.5 μm at +285.51 and +385.27 days postexplosion. These nebular spectra are dominated by asymmetric emission lines from atomic species including H, Ca, Ar, C, Mg, Ni, Co, and Fe, indicative of an aspherical explosion. The other strong features are molecular CO vibrational bands from the fundamental and first overtone. We introduce a novel, data-driven approach using non-local thermodynamic equilibrium three-dimensional (3D) radiative transfer simulations to model the CO emission with high fidelity. This method enables us to constrain the 3D CO distribution and its radial temperature structure. CO formation is found to occur prior to day +285, with subsequent evolution characterized by progressive evaporation. The CO mass decreases from approximately 8.7 to $1.3 \times 10^{-3} M_{\odot}$, while the average temperature drops from ≈ 2900 to ≈ 2500 K. Concurrently, the CO distribution transitions from nearly homogeneous to highly clumped (density contrast increasing from $f_c \approx 1.2$ to 2). The minimum velocity of the CO-emitting region remains nearly constant ($v_1 \approx 1200$ to 1100 km s^{-1}), significantly above the receding photosphere velocity ($v_{\text{ph}} \approx 500 \text{ km s}^{-1}$), suggesting the photosphere resides within Si-rich layers. However, the temperature profile indicates that only a narrow zone reaches the conditions necessary for SiO formation. Due to a lack of observational constraints, SiO clumping is not modeled, and thus, synthetic SiO profiles for mass estimates are not highlighted. We discuss the implications of these findings for dust formation processes in SN 2024ggi.

Unified Astronomy Thesaurus concepts: [Type II supernovae \(1731\)](#)

1. Introduction

The origin of cosmic dust in the early Universe remains a central question in astrophysics, with supernovae (SNe) frequently cited as key contributors (e.g., E. Dwek & J. M. Scalo 1980; D. H. Wooden et al. 1993; R. Schneider et al. 2004; E. Dwek 2006; C. Gall et al. 2011). Although theoretical and observational studies support their role,

significant uncertainties persist regarding the quantity, composition, and grain size distribution of dust produced by various types of SNe. At the heart of this process lies molecular formation, which precedes dust condensation and plays a critical role in cooling the expanding ejecta (W. Liu & A. Dalgarno 1995; S. Liljegren et al. 2020). These molecules not only provide nucleation sites for dust grains but also regulate the thermal evolution necessary for the gas-to-dust transition (A. Sluder et al. 2018).

Obtaining multiwavelength spectra covering the near- and mid-infrared (NIR and MIR, respectively) at wavelengths between 2.5 and 25 μm of molecule-emitting regions in hydrogen-rich core-collapse supernovae (SNe II) has historically been challenging. Nevertheless, several studies have confirmed the presence of freshly formed CO and SiO in the

¹⁹ NHFP Einstein Fellow.

²⁰ National Science Foundation Graduate Research Fellow.



ejecta of SNe II (P. F. Roche et al. 1991; D. H. Wooden et al. 1993; R. Kotak et al. 2006, 2009; T. Szalai et al. 2011). The CO first overtone at $2.2\ \mu\text{m}$ has been the most frequently detected molecular feature, owing to its accessibility with ground-based NIR spectroscopy (J. Spyromilio & B. Leibundgut 1996; W. P. S. Meikle et al. 2011; S. Davis et al. 2019; J. Rho et al. 2021; K. Medler et al. 2025). In contrast, detections of the SiO fundamental band at $\sim 8.1\text{--}9.3\ \mu\text{m}$ have been limited to a handful of events observed with the Spitzer Space Telescope (R. Kotak et al. 2005; T. Szalai et al. 2011). Observations of the CO fundamental band remain especially scarce; aside from SN 1987A (D. H. Wooden et al. 1993), most detections are incomplete or only marginally constrained due to limited MIR spectral coverage (R. Kotak et al. 2005; T. Szalai et al. 2011). The James Webb Space Telescope (JWST) has begun to provide panchromatic observations of SNe II, spanning $0.4\text{--}25\ \mu\text{m}$ (M. Shahbandeh et al. 2024; E. Baron et al. 2025; J. M. DerKacy et al. 2025; K. Medler et al. 2025). This unprecedented wavelength coverage rapidly transforms the study of molecule and dust formation by allowing the regions of the first overtone and fundamental vibrational bands of CO and SiO to be simultaneously observed at high sensitivity and spectral resolution.

SN 2024ggi, classified as an SN IIP with flash ionization features (W. Hoogendam et al. 2024; Q. Zhai et al. 2024), was discovered on 2024 April 11 (MJD 60411.14, S. Srivastav et al. 2024) in the host galaxy NGC 3621, located at a distance of 7.24 ± 0.20 Mpc (A. Saha et al. 2006). Its proximity makes it an ideal candidate for monitoring and tracking the evolution of molecule formation in SN II explosions.

Here we present JWST observations of SN 2024ggi from our JWST Director’s Discretionary (DD) programs DD-6616 and DD-6717 (C. Ashall et al. 2024a, 2024b). This program aimed to follow the infrared spectral evolution of SN 2024ggi from the plateau to the nebular phase.

The first epoch of observations, which consists of $1.5\text{--}14\ \mu\text{m}$ spectra, observed at 55 days past explosion, was presented in the first paper of this series (E. Baron et al. 2025). These observations were obtained during the plateau phase and before the formation of CO, which can be expected when the photosphere enters the C/O-rich core (P. Höflich 1988; J. Spyromilio et al. 1988; S. J. Petuchowski et al. 1989; W. Liu et al. 1992; C. L. Gerardy et al. 2000, 2002; R. Kotak et al. 2005; M. Shahbandeh et al. 2023). Here we concentrate on the next two epochs obtained at $+285.64$ and $+385.55$ days past the explosion. The purpose of these observations is to investigate the formation and evolution of CO within the ejecta.

In Section 2, we present the observations and describe the data reduction procedures. This is followed in Section 3 by our analysis of the spectra, including line identifications, velocity measurements of key features, and spectral comparisons. In Section 4, we introduce multidimensional non-local thermodynamic equilibrium (non-LTE) models of the CO-emitting regions. Finally, our discussion and conclusions are presented in Section 5.

2. Data Reduction

We obtained two epochs of data with JWST’s Near-Infrared Spectrograph (NIRSpec; P. Jakobsen et al. 2022; T. Böker et al. 2023) as part of our program, on 2025 January 22

(MJD = 60697.13) and 2025 May 2 (MJD = 60797.29), corresponding to $+285.64$ and $+385.55$ days after the inferred explosion date of MJD = 60410.795 (W. V. Jacobson-Galán et al. 2024).

For these observations, we used the F170LP/G235M and F290LP/G395M filter/grating combinations, providing spectral coverage from $1.66\text{--}3.07$ and $2.87\text{--}5.10\ \mu\text{m}$, respectively, at a resolving power of $R \sim 1000$. We performed the observations with the S400A1 slit, the SUBS400A1 subarray, the NRSRAPID readout pattern, 40 groups per integration, and a three-point nod dither pattern with offsets of the position Y of $+0.9845, 0''$, and -1.1952 .

The reduction process followed standard procedures outlined in the NIRSpec fixed-slit Jupyter notebooks (D. Law et al. 2025), using `jwst` pipeline version 1.18.0 (H. Bushouse et al. 2025a, 2025b), Build 11.3, and the `jwst_1364.pmap` CRDS calibration files. We adjusted standard reduction parameters to include a scaling factor in the `outlier_detection` step during stage 3 spectroscopic processing, reducing noise spikes caused by bad pixels in the three dithers while preserving source flux. We used total exposure times of 191.695 and 472.135 s for observations at $+285.64$ and $+385.55$ days, respectively.

3. Spectral Properties

3.1. Line Identification

Figure 1 shows both epochs of our JWST observations. In these phases, SN 2024ggi has entered the nebular stage, with spectra dominated by strong emission lines. We identify the spectral features in SN 2024ggi using previously published line lists from A. Jerkstrand et al. (2012), S. Davis et al. (2019), and M. Shahbandeh et al. (2022). The spectra exhibit numerous hydrogen lines, including $\text{Pa}\alpha$ ($1.875\ \mu\text{m}$), $\text{Br}\alpha$ ($4.051\ \mu\text{m}$), $\text{Br}\gamma$ ($2.166\ \mu\text{m}$), $\text{Br}\beta$ ($2.626\ \mu\text{m}$), $\text{Br}\epsilon$ ($1.817\ \mu\text{m}$), $\text{Br}\delta$ ($1.944\ \mu\text{m}$), $\text{Pf}\delta$ ($3.297\ \mu\text{m}$), $\text{Pf}\gamma$ ($3.741\ \mu\text{m}$), and $\text{Pf}\beta$ ($4.654\ \mu\text{m}$). We also identify additional lines from ions such as He I ($1.7002\ \mu\text{m}$, $2.0581\ \mu\text{m}$), Na I ($2.206\ \mu\text{m}$), Mg I (2.486 , 3.867 , and $4.201\ \mu\text{m}$), [O I] ($2.763\ \mu\text{m}$), [C I] ($3.565\ \mu\text{m}$), [Fe II] (1.809 , 3.029 , and $4.075\ \mu\text{m}$), [Co II] ($3.286\ \mu\text{m}$), [Ni II] (1.985 , 2.911 , $3.119\ \mu\text{m}$), and [Ni III] ($3.393\ \mu\text{m}$).

Broad emission features spanning $2.2\text{--}2.4$ and $4.5\text{--}5.17\ \mu\text{m}$ trace the first overtone and fundamental vibrational bands of CO, respectively. Although the first CO overtone has been detected in many SNe (e.g., S. Davis et al. 2019; J. Rho et al. 2021), observations of the CO fundamental band remain rare due to the historical lack of spectroscopic coverage in the $2\text{--}5\ \mu\text{m}$ range. To date, the only published detections of the full fundamental CO band in an SN II are SN 1987A and SN 2023ixf (D. H. Wooden et al. 1993; K. Medler et al. 2025).

Over the ~ 100 days between our two JWST epochs, the spectra evolve significantly. The hydrogen emission lines decline in flux, while the lines from intermediate-mass and iron-group elements become relatively stronger. The CO emission features also weaken over this period. Notably, the shape of the CO first overtone band evolves: higher vibrational modes fade relative to the first epoch, indicating a decrease in the temperature of the CO-emitting region (we explore this further in Section 4). The fundamental band of CO also fades, but only by $\sim 50\%$ in absolute flux, in contrast to the order-of-magnitude decline observed in the first overtone. This suggests

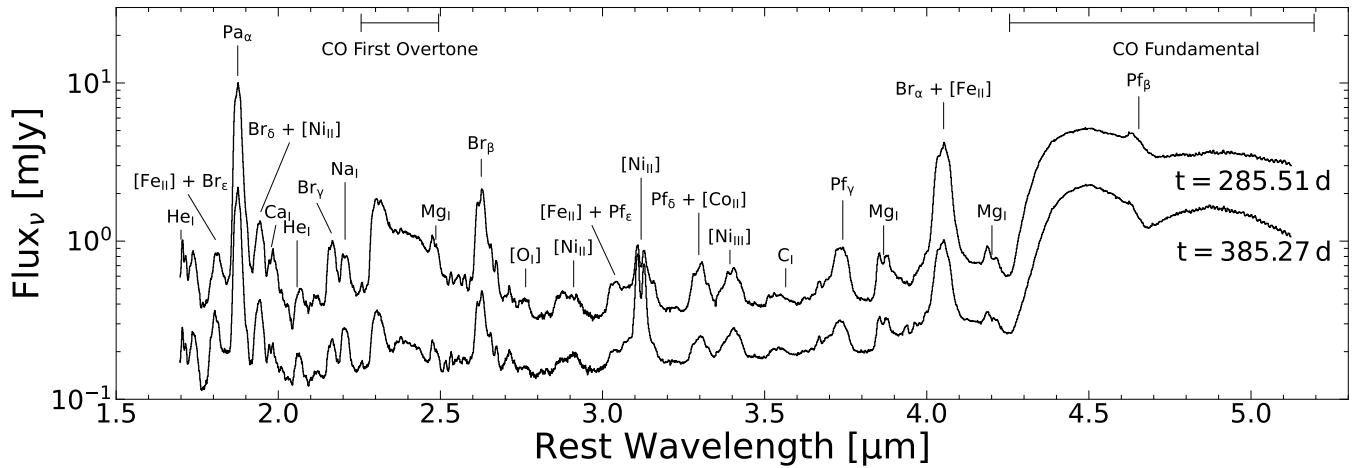


Figure 1. Our NIRSPEC observations of SN 2024ggi at +285.64 and 385.55 days past explosion. We identify the prominent spectral features.

that the fundamental CO band becomes a dominant coolant in the ejecta at later times.

3.2. Spectral Line Velocities

Figure 2 shows the spectral line velocity profiles of the most prominent features at both epochs. The hydrogen profiles span ± 5000 km s $^{-1}$ and show no attenuation on the red side, indicating the absence of dust within the ejecta (L. B. Lucy et al. 1989). In fact, the Br α , Br γ , and Pa α lines, which are isolated, exhibit tilted profiles with a peak on the red side at ~ 1000 km s $^{-1}$, suggesting an asymmetric chemical distribution. However, the expansion velocity of these features is large, causing the profiles to blend.

Looking at the intermediate-mass and iron-group elements (see the right-hand panel of Figure 2), we observe clear evidence of splitting in all isolated features. This is most prominent in the [Ni II] 3.119 μ m feature, which is split by 1000 ± 150 km s $^{-1}$, as well as in the three Mg I features, which show slightly broader lines. The splitting of these spectral features in SN 2024ggi is consistent with the optical nebular phase, where similar splitting of the Fe group lines is observed (L. Ferrari et al. 2025; E. Hueichapán et al. 2025). The splitting may be due to the ejecta being in an oblate or torus-like configuration or due to jetlike structures from the explosion (see e.g., A. M. Khokhlov et al. 1999; P. A. Mazzali et al. 2005; K. Maeda et al. 2008; M. Modjaz et al. 2008; L. Dessart & D. J. Hillier 2011). Overall, the splitting of the lines and attenuation of the red side of the flux in the emission features related to stellar or explosive burning suggest that SN 2024ggi is an asymmetric explosion with little to no mixing between the ^{56}Ni layers and the C/O-rich regions.

3.3. Spectral Comparison

In Figure 3 we compare our JWST spectra of SN 2024ggi to those of SN 1987A and SN 2023ixf, the only other SNe II with published spectral data covering this wavelength range (D. H. Wooden et al. 1993; K. Medler et al. 2025). Overall, the spectra are remarkably similar, both dominated by emission lines from the same atomic species and by prominent CO emission. Like SN 2023ixf, JWST data for SN 2024ggi were obtained at significantly higher spectral resolution, allowing us to resolve features that remained mixed in SN 1987A. For example, in SN 2024ggi we clearly resolve the [Ni II] and [Ar II]

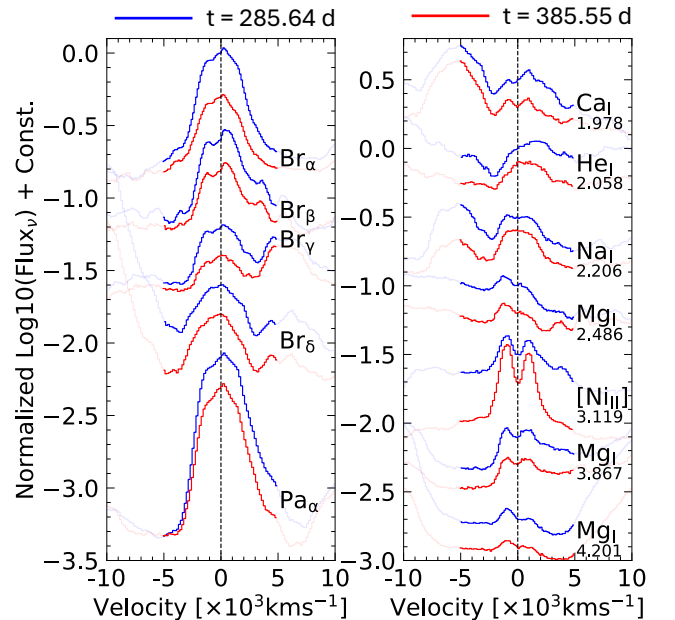


Figure 2. Spectral line profiles of the strongest ions on the nebular phase spectra of SN 2024ggi. Various hydrogen profiles are shown in the left panel, while lines of other elements are presented in the right panel.

lines near 3.1 μ m, which appear to be blended in the SN 1987A dataset.

The most notable difference between these objects lies in the CO first overtone region. In SN 1987A, the blueward extension of this feature includes CO $^+$ emission. This is most likely due to mixing between ^{56}Ni and the C/O-rich layers and excitation by the emitted gamma rays (J. Spyromilio et al. 1988; S. J. Petuchowski et al. 1989; J. Rho et al. 2021). We find no evidence of CO $^+$ emission in SN 2024ggi, suggesting that ^{56}Ni is likely not significantly mixed in the CO-forming layers.

4. Molecular Models

In the following, we analyze the spectral features of CO and their evolution over time. Our goals are to (a) quantify the abundance of diatomic molecules, (b) assess the physical conditions of the corresponding stellar layers, including their abundance, temperature, and distribution, and (c) investigate

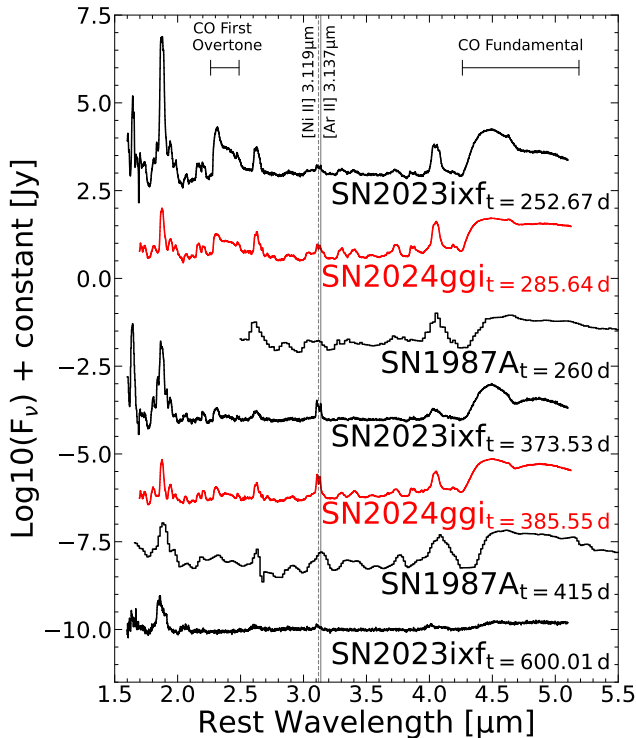


Figure 3. 1.5–5.5 μm spectral comparison between SN 2024ggi, SN 1987A, and SN 2023ixf. The SN 2023ixf spectra have been continuum subtracted following the procedure of Figure 4 in K. Medler et al. (2025) to aid in visual comparison.

the small-scale three-dimensional (3D) morphology of CO and use it to constrain details on the stellar progenitor and dust formation.

Frequently, diatomic molecules are analyzed under the assumption that their features are optically thin, with a constant temperature and total mass adjusted to best fit the observed data (D. P. K. Banerjee et al. 2018; M. D. Stritzinger et al. 2024; S. H. Park et al. 2025). This treatment breaks down for the optically thick fundamental bands and at later times when non-LTE effects are important (W. Liu et al. 1992).

To overcome this shortcoming, other works have employed forward modeling, combining explosion models with the time evolution of molecular formation to produce spherical non-LTE synthetic spectra (e.g., P. Höflich 1988; W. Liu et al. 1992; W. Liu & A. Dalgarno 1994; R. Kotak et al. 2005; J. Rho et al. 2021; C. McLeod et al. 2024). For some SNe, this approach provides reasonable results for the CO first overtones (see, e.g., SN 1987A, P. Höflich 1988; J. Spyromilio et al. 1988; W. Liu et al. 1992 and SN 2000ew C. L. Gerardy et al. 2002), as well as for the optically thin part of the CO fundamental band (see models of SN 2005df in R. Kotak et al. 2005). However, in other SNe, such as SN 1987A, the profiles and synthetic flux levels of the CO fundamental band to the first overtone are inconsistent by factors of 2 to 5 (see Figure 12 in C. McLeod et al. 2024). This discrepancy suggests some fundamental shortcomings, including lack of understanding on how the molecules contribute to the overall temperature structure and of how multidimensionality effects the molecular forming layers (S. Liljegren et al. 2020). Additionally, forward modeling based on spherical geometries is inherently incapable of resolving the underlying multidimensional physics.

Thus, we developed an inverse-data-driven approach to analyze the unique spectra only obtainable with JWST. Namely, we use the observed absolute flux, combined with full radiation transport that includes small-scale 3D morphology effects (clumping) in a homologously expanding envelope, to calculate the cooling structure by molecules and, with it, the temperature profile of the molecular layers. In turn, this can be used to constrain the underlying physical mechanisms that drive molecular formation. This approach has been implemented in our newly developed MOlecular Fitting Analysis Tool (MOFAT) code (T. Mera et al. 2025), which allows us to analyze the observed diatomic features.

4.1. Method for the Analysis

MOFAT consists of a seven-parameter iterative framework that utilizes the observed flux in molecular bands and finds the optimal solutions in the multidimensional parameter space. It uses physics-based modules to provide an on-demand solution for physical structures associated with the signatures of molecules formed. At its core, MOFAT assumes spherically symmetric large-scale geometry and uses a solution of the radiation transport equations that includes the effects of multidimensional clump-like structures. Molecular opacities are calculated by HYDRA (C. M. Sharp & P. Höflich 1989; C. M. Sharp & P. Höflich 1990; P. Höflich et al. 2002; P. Höflich et al. 2021; J. Rho et al. 2021), where the vibrational bands within each mode are treated with non-LTE correction factors (R. R. Gamache & L. S. Rothman 1992; W. Liu et al. 1992; L. S. Rothman et al. 2010). Unlike HYDRA, which solves the time-dependent rate equations for the formation of molecules, MOFAT takes critical parameters associated with the CO profiles and then uses observations as the driver toward an optimized solution at a particular time (see T. Mera et al. 2025 for a full description of MOFAT and Table 1 for a description of the parameters).

In general, the starting conditions of our models begin with the overall properties of the SN derived from observations. The time since the explosion is taken from the light curves, and the photosphere expansion velocity, v_{photo} , and effective temperature, T_{eff} , can be estimated from optical spectra (see, e.g., R. P. Kirshner & J. Kwan 1974; K. Takáts & J. Vinkó 2012; S. Bose & B. Kumar 2014; W. Hoogendam et al. 2024). Additionally, when our spectra are analyzed, the distance to the object is taken at the currently accepted value, but we note that the distance uncertainties will propagate directly to CO mass uncertainties.

The temperature structure, $T(\nu)$, in the molecular-rich region with expansion velocities $\nu \in [\nu_1, \nu_1 + \Delta\nu]$ is obtained under the assumption of radiative equilibrium being established by the cooling and heating of molecules (and dust). Finding $T(\nu)$ by the formal solution requires partial derivatives for all parameters. However, the seven-dimensional (7D) parameter space of MOFAT would make this method unstable. Instead, for any given set of parameters, the “optimal” temperature structure is calculated using a data-driven approach. Optimal means that $T(\nu)$ is found such that $\int \chi^2(\lambda) d\lambda$ between the observed and synthetic profiles is minimal. $T(\nu)$ at the inner boundary of the molecular region ν_1 is determined by the observed photospheric spectrum. The temperature at the outer boundary is calculated under the assumption that the observed total flux in the molecular and dust bands is produced in the corresponding region for a given set of parameters. Within the

Table 1
Parameter Values from Figures 4 and 5 Optimized for the Two Epochs Observed

Model	Time (day)	Clumps	Mass (M_{\odot})	T_1 (K)	v_1 (km s $^{-1}$)	Δv (km s $^{-1}$)	n	r/R	f_c	ϵ
P	285	yes	8.72e-3	2469	1240	3280	6.04	1.80e-1	1.16	70
	385	yes	1.31e-3	1951	1050	3700	6.64	1.38e-1	1.83	14
O	285	yes	8.88e-3	2423	1200	3210	6.86	1.72e-1	1.19	0.08
	385	yes	1.62e-3	1828	1130	3500	5.14	1.58e-1	1.89	0.46
S	285	no	3.90e-3	2883	1100	3180	7.00
	385	no	5.81e-4	1944	893	3130	11.0
E1	285	yes	9.48e-3	2469	1240	3280	6.04	2.00e-1	1.16	70
	385	yes	1.35e-3	1951	1050	3700	6.64	1.38e-1	2.00	14
E2	285	no	1.52e-3	2883	1300	3180	7.00
	385	no	8.28e-4	1944	893	3130	7.00

Note. Models P and O indicate the best-fitting models for prolate and oblate clumps. Models S are without clumps and provide a reasonable fit to the early epoch (see the text). To demonstrate the sensitivity on the parameters, Models E1 and E2 are given as examples. The Clumps column indicates whether the model takes into account clumping effects. The Mass column shows the total amount of CO mass. T_1 shows the temperature at the inner edge (v_1) of the CO shell, which has a width of Δv . n is the slope of the CO density distribution. r/R is the relative size of the clumps with respect to the radius. f_c is the density enhancement factor within the clump with respect to its environment. ϵ is the flattening parameter of the spheroid shape of the clump (when $\epsilon = 1$ it is a sphere, <1 an oblate, and >1 a prolate). Based on theoretical models (P. Hoefflich 1988; L. Dessart & D. J. Hillier 2005), the photosphere is formed at $\lesssim 10^{15}$ cm, corresponding to $v_{\text{ph}} \lesssim 500$ km sec $^{-1}$, which is consistent with early time observations of SN 2024ggi (K. Ertini et al. 2025), and well below v_1 .

region, $T(v)$ is governed by radiative equilibrium, namely, that the luminosity is balanced by the emissivity in each zone. However, we utilize $T(v) = T(v_1) + C \Delta T(v)$ to force agreement with the flux observed at the outer boundary. This allows for a direct comparison between observed and synthetic line profiles and gauges the quality of the fits using χ^2 . C is needed to compare the quality of profile fits, though C for a given set may be unphysical. That said, this procedure allows us to find the 7D parameter set with the minimum χ^2 . Note that for the optimized solution of the full problem, C approaches unity with a dispersion comparable to the noise in the observations.

The optimal set of free parameters related to the molecular features is found by a fixed-point iteration in a 7D parameter space using a nested iteration scheme, with the order determined by the spectral tell-tails.

From the overtone, we find a temperature T_1 (defined at v_1) that best matches the observations because for optically thin features the inner high-density region dominates the emission. The overtone will also indirectly determine the total CO mass when we have a value for the slope, n , of the CO density distribution ($\rho \sim r^{-n}$). Throughout the envelope, the CO cooling is dominated by the fundamental band and drives ΔT at the outer boundary. For the inner loops, properties of the clumps are used. We define our clumps as spheroids, where we can specify their morphology with three parameters: (1) r/R is the relative size of the clumps with respect to any given radius in the envelope, (2) f_c is the density enhancement factor within the clump with respect to its environment, and (3) ϵ is the flattening parameter of the spheroid (when $\epsilon = 1$ it is a sphere, <1 an oblate, and >1 a prolate). Oblate and prolate structures will have different surface-to-volume ratios and, thus, will have varying levels of absorption and emission. We will optimize our fits within both regions because they can have different physical interpretations. We note that the overtone can be fitted by a range of clumping parameters for each time, but the profiles of the fundamental bands cannot. Nonconsistent parameters reveal themselves by failed fits of the fundamental (see below). MOFAT iterates all seven

parameters until we converge on a set that best matches the observations.²¹

4.2. Analysis of the Molecular Features

In Figures 4 (models P and O) and 5 (model S), we show our best fits of both the fundamental and overtone CO bands for SN 2024ggi for prolate, oblate, and nonclumping models, respectively, at +285 and +385 days. E1 and E2 are given as examples for clumped and nonclumped models where their parameters fail to fit the profile despite temperature structure convergence based on a consistent molecular cooling function. The model parameters are given in Table 1.

Several properties are common between all models shown: the CO mass decreases by a factor of ≈ 8 between observations, the location of the CO-rich region in velocity space is very similar at either time, the minimum velocity, v_1 , only slightly decreases with time, and the reference temperature, T_1 , decreases with time, with overall differences between the temperature profiles shown in Figure 6. The temperature minimum is mainly caused by the cooling of the optically thick fundamental band. Further out, T rises due to the fundamental band becoming optically thin from the increasing blueshift and geometrical dilution allowing for more exposure to intense radiation from the inner ejecta. This increases the heating of the inner CO layers and the dissociation of CO and provides a possible explanation for the CO destruction. Full radiation hydro models that included CO formation show that most of the CO is formed close to the photosphere (at temperatures around $T_1 \approx 5000$ K) with CO freely expanding with ejecta (P. Höflich 1988; J.-C. Gérard et al. 2000; J. Rho et al. 2021). Together with the reference temperature being much smaller than the formation temperature, the decreasing mass of CO, and the inner velocity only slightly decreasing, this suggests that the CO formation has

²¹ Solutions with reasonable parameters are clustered tightly.

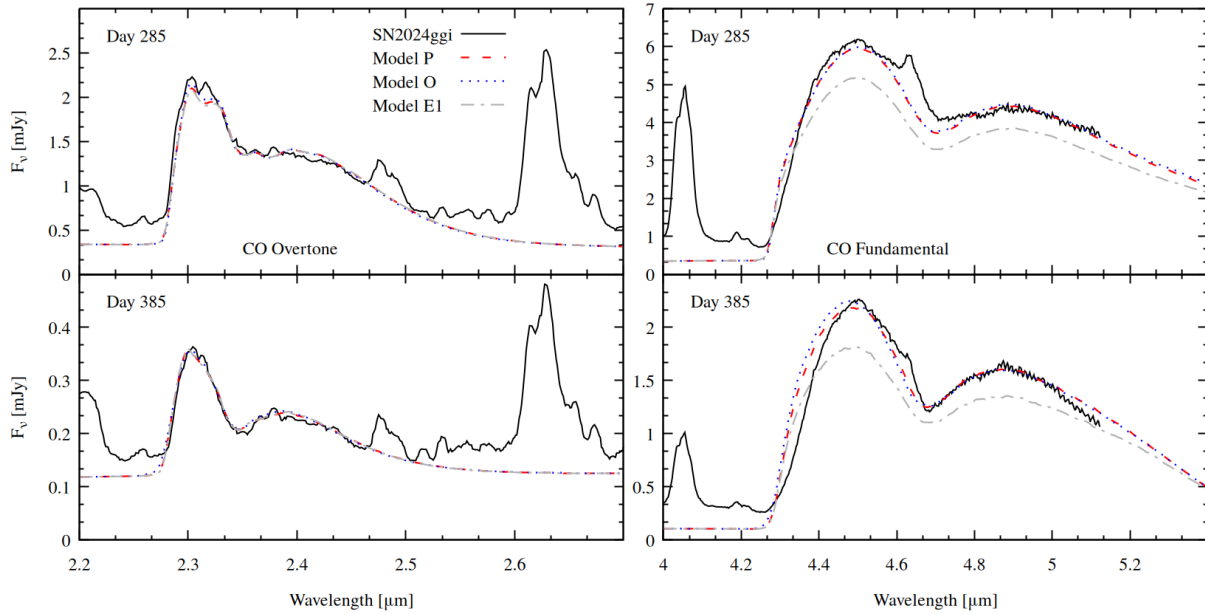


Figure 4. Comparing our prolate (P) and oblate (O) clumping models to the observations of SN 2024ggi. The upper panels show our results at 285 days, and the bottom panels show our results at 385 days. Our best-fit models (P and O) are in dashed red and dotted blue, respectively, and we show the sensitivity of the parameters with the models defined with E1 (dotted–dashed gray). We vary the clumping size (r/R) at 285 days and the density enhancement (f_c) at 385 days. See Table 1 for the complete list of model parameters and Figure 6 for the temperature structure of the best fits.

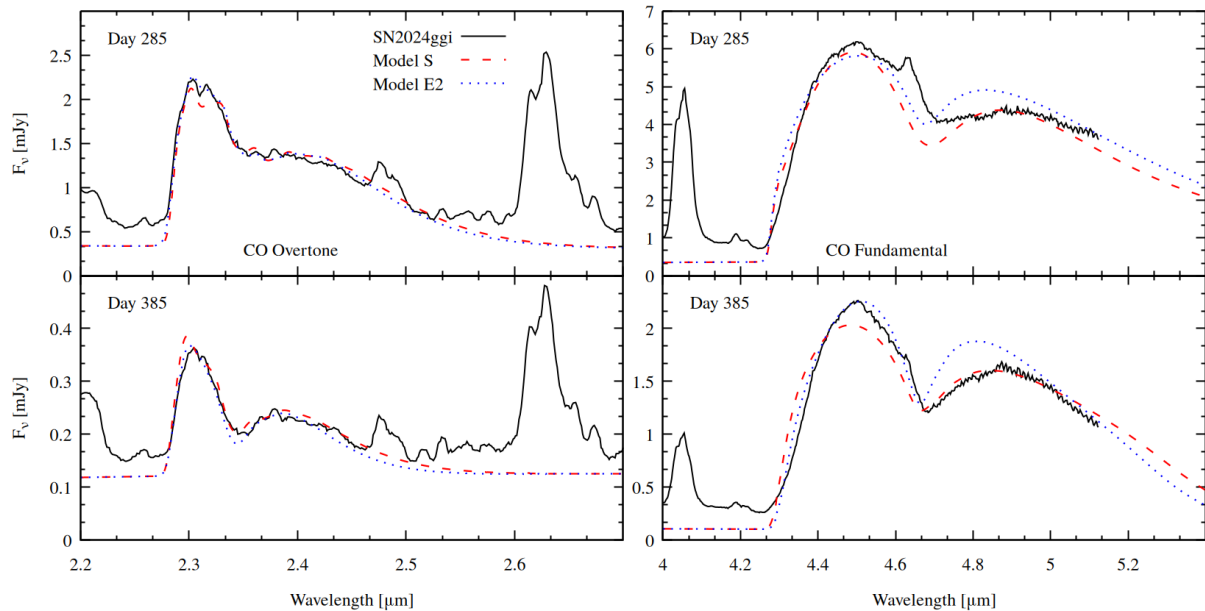


Figure 5. Same as Figure 4 but for models without clumps.

mostly stopped by day 285 and that the photosphere has receded to the carbon-poor, Si-rich layers of the explosion.

We find good overall agreement in the fits of clumping and nonclumping models at 285 days (Figure 4 for P and O and Figure 5 for S), but only P and O allow for a good reproduction of the fundamental band at the later date. At each epoch, the CO overtone can be reproduced in all examples, demonstrating the need for the MIR observations to separate optically thin, one-temperature models to those that include optical depth effects. One exception is the small dip at $2.31 \mu\text{m}$ in the vibrational modes of the overtone. This dip is present in our simulations and is produced by either self-absorption in

solutions that are barely optically thick or by varying degrees of temperature decoupling between the vibrational and rotational bands. Similar structures have been seen in SN 1987A (W. Liu et al. 1992). The feature at $4.65 \mu\text{m}$ is the $\text{P}\beta$ and is not included in our fits (see Figure 1).

Note that at +285 days the minimum temperature by CO cooling is slightly above 2000 K in a narrow range for our clumping models (see Figure 6). This temperature is approaching the onset of SiO formation (see Figure 18 of J. Rho et al. 2021). By +385 days the minimum temperature is below 2000 K, but at this T , only little Si will be bound in SiO, which would be insufficient to effectively cool. If we assume

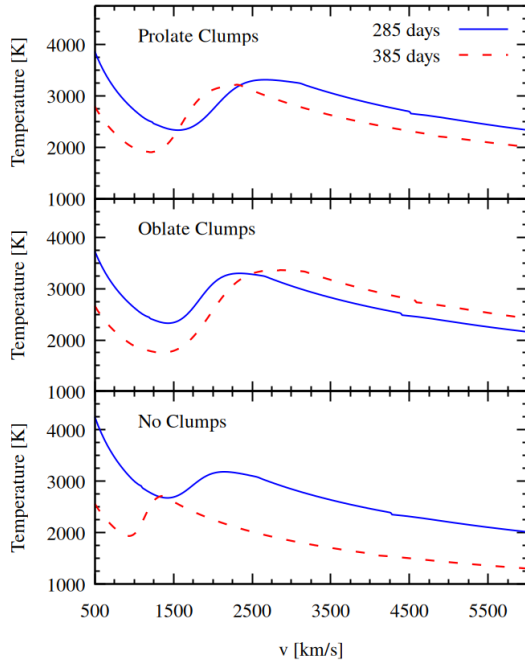


Figure 6. Converged temperature structures of gas with optimized parameters with and without clumps. In the upper panel, we show the prolate clumping model P. The middle panel shows the oblate clumping model O. The lower panel shows the nonclumping model S. See Table 1 for the model parameters and Figures 4 and 5 for their fits.

equilibrium abundance based on the $15M_{\odot}$ stellar model with solar metallicity from A. Chieffi et al. (2003) and take the temperature profiles of model P, we would expect to find some 6.3×10^{-4} and $1.5 \times 10^{-3}M_{\odot}$ of SiO at +285 and +385 days, respectively. In Figure 7, we give synthetic spectra of the SiO fundamental band using these mass estimates in a narrowed molecular region.

The similarity between the clumping and nonclumping models early on can be understood by the fact that the overdensity in O and P is small ($f_c \approx 1.2$), essentially approaching the nonclumping solution ($f_c = 1$). The fact that the converged parameters between the models only differ by approximately 10% suggests that clumps are not significant until times later than 285 days.

At 385 days, we find consistent agreement between the clumping models and the observations of SN 2024ggi but found poor agreement for our converged nonclumping model (see Figure 7 for a direct comparison). In detail, Model S shows significant shortcomings in the fundamental band, namely, the flux ratio between the first and second vibration modes at later times is about 15% smaller than the observation, an increase from $\approx 5\%$ at earlier times due to optical depth effects. More precisely, in smooth distributions the ratio between the opacities of the first and second mode and the radii at which they become optically thin make their flux ratio stable. In clumpy media, the emission is formed over a wide range (“picket fence”), and thus, it depends sensitively on the morphology and overdensity of the clumps providing a sensitive diagnostic. Because models with clumps converge early on and are needed at later time, we always include clumps as free parameters and discuss their evolution.

For both O and P models, there is a tendency for the clumps to become smaller and rounder with increasing density contrast f_c . With time, CO in the outer layers of the clumps becomes

dissociated by SN radiation (see above), leading to both rounder and smaller clump sizes. The higher f_c is suggested by the pressure equilibrium between the heated outer and the cool central layers. The two dates are insufficient to distinguish oblate and prolate structures.

We have demonstrated the utility of the inverse-data-driven method of analysis. For future observations, low-latency observations are needed to evaluate the process of CO formation right after the onset, namely, the end of the plateau phase, the subsequent formation of SiO, and at later times to answer whether molecule formation is the trigger of dust formation in SNe.

5. Conclusions

We present NIRSpec JWST data of SN 2024ggi during the nebular phase at +285.64 and +385.55 days postexplosion, obtained as part of our DD Program 6717 (C. Ashall et al. 2024b). The main results of the paper are as follows:

- (1) The spectra are dominated by atomic emission lines from H, Ca, Ar, C, Mg, Ni, Co, and Fe. These lines exhibit asymmetry, suggesting an asymmetric chemical distribution in SN 2024ggi (Figure 3 and Section 3).
- (2) The spectra also reveal clear signatures of CO through the emission of flux from the first overtone and fundamental bands (Section 3).
- (3) We presented a new, data-driven approach that directly targets the properties of the ejecta with molecules (T. Mera et al. 2025) using non-LTE transport simulations to calculate the temperature structure in the molecular-rich region of the ejecta. We discussed the sensitivity of this method to detect and characterize inhomogeneities (Section 4), which allows us to decipher the complex 3D structure and reproduce detailed high-fidelity profiles. This approach fundamentally differs and overcomes the two classical approaches which are (I) assuming one-zone models with a given temperature in the optically thin case, which is not valid for the fundamental molecular band, and (II) the forward approach that calculates the full explosion in spherical geometry. Though justified for the formation of CO, it fails to capture the complexity of the physics seen at later times (Section 4.2).
- (4) The CO first overtone is mostly optically thin at both dates. MIR spectra (i.e., JWST) are crucial for deciphering the structure and provide stable mass estimates for molecules. However, a small inversion on top of the overtone band is reproduced as an optical depth combined with a non-LTE effect in the CO-cooling region. (Figures 4 and 5).
- (5) At +285 days, the model parameters indicate large-scale, almost homogeneous CO distributions. Both models with and without small-scale structure give reasonable fits to the data, with higher quality requiring clumps. The spectrum at +385 days clearly demonstrates the importance of clumps and the need for spectral series (Section 4.2 and Figure 7).
- (6) The majority of CO formation is before +285 days, and the subsequent phase is characterized by CO destruction from $M_{\text{CO}}(+285 \text{ days}) \approx 9 \times 10^{-3}$ to $M_{\text{CO}}(+385 \text{ days}) \approx 1.5 \times 10^{-3}M_{\odot}$. In our models, this can be attributed to the rising temperature caused by energy input from inner layers because Doppler shift and geometrical dilution exposes CO to harder radiation and heating (Figure 6 and Section 4.2).

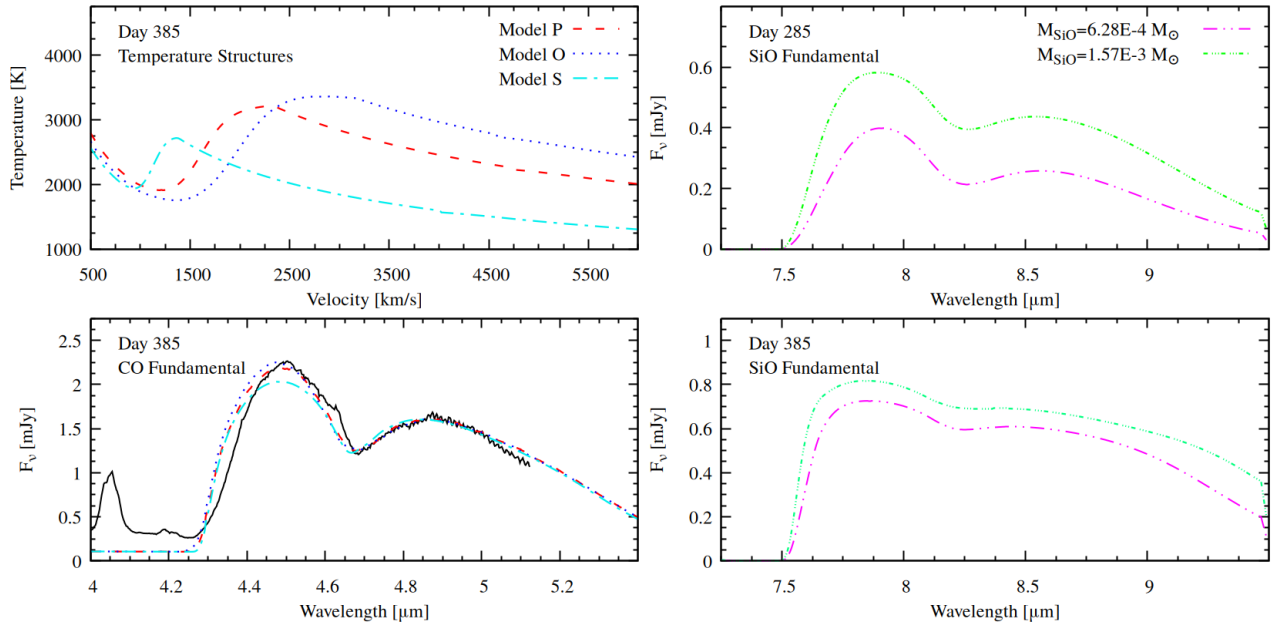


Figure 7. We compare the temperature profiles of the best-fit models at +385 days in the upper-left quadrant. In the lower-left panel we compare the fundamental CO band of the models with and without clumps at +385 days. Without clumps, the ratio between the first and second vibrational modes of the fundamental band are off by $\approx 15\%$. In addition (upper- and lower-right quadrants), we give synthetic SiO fundamental profiles using the temperature structures of Model P (Figure 6) at +285 and +385 days, respectively. We use equilibrium abundances based on the $15 M_{\odot}$ stellar model with solar metallicity (A. Chieffi et al. 2003) and find that most of the Si exposed is in atomic Si and only some 6.3×10^{-4} and $1.5 \times 10^{-3} M_{\odot}$ are in SiO at +285 and +385 days, respectively. For the synthetic spectra we do not include clumping and use $n = 1.1$, $v_1 = 900 \text{ km s}^{-1}$ and $\Delta v = 900 \text{ km s}^{-1}$ at both epochs. We did not demonstrate parameter differences because Si- and C-rich layers can be expected to have different clump structures, and we assumed equilibrium for the SiO estimate.

- (7) The clumps in our models are optically thick in the fundamental band, leading to smaller and rounder clumps as CO is destroyed, where the pressure equilibrium between the hot outer and cool inner layers increases the density enhancement factor (f_c) (Table 1).
- (8) The inner edge of the CO-rich region is well above the photosphere at both epochs, suggesting that the photosphere has entered the region of advanced burning stellar products. From model-based estimates we might expect to find $M_{\text{SiO}} \approx 6.3 \times 10^{-4}$ and $1.5 \times 10^{-3} M_{\odot}$ at +285 and +385 days, respectively (Figure 7). Although masses of this level would be insufficient to reasonably cool the ejecta, we suggest that more SiO will be formed at later times and may trigger additional cooling leading to dust formation.

Finally, we also have to mention the shortcomings. Early time observational coverage after the plateau phase would be needed to study the formation process and to link the CO-rich layers to the explosion physics, e.g., by the observation of ionized molecules (J. Spyromilio et al. 1988; J. Rho et al. 2021). Later times with good time coverage are needed to probe the phase of strong SiO formation with additional cooling. This is needed to establish molecular formation as a trigger for dust formation. From theory, an extended study of the sensitivity on the various parameters is underway to develop further diagnostics, e.g., linking the SiO bands and their appearance to the progenitor and explosion physics. Taking the new constraints from above, it is tempting to employ complex multidimensional simulations that use a forward approach, but SNe II are a very diverse group of objects, so, a large grid of models and many well-sampled SNe II would be needed to understand the growth and cooling of small-scale 3D structures.

Overall, we have demonstrated that JWST spectral observations of SNe II can be used to infer the 3D geometry of the molecule-

forming regions. In the case of SN 2024ggi, clumping is required to simultaneously reproduce both the CO first overtone and fundamental band. Such clumping may be a common feature in all SN II explosions. Looking ahead, time-series spectral observations beginning shortly after an SN II exits the plateau phase would allow for direct tracking of both the growth of CO mass and the evolution of clumping within the ejecta.

Acknowledgments

We thank the director of the Space Science Institute for granting time for these observations. T.M., K.M., E.B., C.A., J. D., M.S., and P.H. acknowledge support from NASA grants JWST-GO-02114, JWST-GO-02122, JWST-GO-04522, JWST-GO-04217, JWST-GO-04436, JWST-GO-03726, JWST-GO-05057, JWST-GO-05290, JWST-GO-06023, JWST-GO-06677, JWST-GO-06213, JWST-GO-06583, and JWST-GO-0923. Support for programs #2114, #2122, #3726, #4217, #4436, #4522, #5057, #6023, #6213, #6583, and #6677 were provided by NASA through a grant from the Space Telescope Science Institute, which is operated by the Association of Universities for Research in Astronomy, Inc., under NASA contract NAS 5-03127.

P.H. and T.M. acknowledge the support by the National Science Foundation NSF awards AST-1715133 and AST-230639 for enabling the development of the methods and computational codes and, in parts, covering the graduate and postdoctorate salaries.

L.G. acknowledges financial support from AGAUR, CSIC, MCIN, and AEI 10.13039/501100011033 under projects PID2023-151307NB-I00, PIE 20215AT016, CEX2020-001058-M, ILINK23001, COOPB2304, and 2021-SGR-01270.

J.T.H. acknowledges support from NASA through the NASA Hubble Fellowship grant HST-HF2-51577.001-A,

awarded by STScI. STScI is operated by the Association of Universities for Research in Astronomy, Incorporated, under NASA contract NAS 5-26555.

W.B.H. acknowledges support from the NSF Graduate Research Fellowship Program under grant No. 2236415.

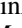
Data Availability

The JWST data for SN 2024ggi were obtained from the Mikulski Archive for Space Telescopes. These observations can be accessed via doi:[10.17909/3v0v-0a76](https://doi.org/10.17909/3v0v-0a76). All other data are available on request.

Facility: The observations were obtained with the JWST. The simulations were performed on the parallel cluster of Florida State University.

Software: MOFAT, part of a PhD thesis, and selective HYDRA modules used in this work are available by request after the PhD thesis is finalized.

ORCID iDs

T. Mera  <https://orcid.org/0000-0001-5888-2542>
 C. Ashall  <https://orcid.org/0000-0002-5221-7557>
 P. Hoefflich  <https://orcid.org/0000-0002-4338-6586>
 K. Medler  <https://orcid.org/0000-0001-7186-105X>
 M. Shahbandeh  <https://orcid.org/0000-0002-9301-5302>
 C. R. Burns  <https://orcid.org/0000-0003-4625-6629>
 E. Baron  <https://orcid.org/0000-0001-5393-1608>
 J. M. DerKacy  <https://orcid.org/0000-0002-7566-6080>
 J. Lu  <https://orcid.org/0000-0002-3900-1452>
 J. T. Hinkle  <https://orcid.org/0000-0001-9668-2920>
 P. A. Mazzali  <https://orcid.org/0000-0001-6876-8284>
 E. Fereidouni  <https://orcid.org/0009-0001-9148-8421>
 C. M. Pfeffer  <https://orcid.org/0000-0002-7305-8321>
 S. Shiber  <https://orcid.org/0000-0001-6107-0887>
 T. Temim  <https://orcid.org/0000-0001-7380-3144>
 L. Galbany  <https://orcid.org/0000-0002-1296-6887>
 D. A. Coulter  <https://orcid.org/0000-0003-4263-2228>
 L. Ferrari  <https://orcid.org/0009-0000-6303-4169>
 W. B. Hoogendam  <https://orcid.org/0000-0003-3953-9532>
 E. Y. Hsiao  <https://orcid.org/0000-0003-1039-2928>
 M. M. Phillips  <https://orcid.org/0000-0003-2734-0796>
 B. J. Shappee  <https://orcid.org/0000-0003-4631-1149>

References

- Ashall, C., Baron, E., DerKacy, J. M., et al. 2024a, Observing Molecule and Dust Formation in the Nearby SN 2024ggi, JWST Proposal, Cycle 2 6677, STScI, 2024jwst.prop.A
- Ashall, C., Baron, E., DerKacy, J. M., et al. 2024b, Observing Molecule and Dust Formation in the Nearby SN 2024ggi, JWST Proposal, Cycle 3 6716, STScI, 2024jwst.prop.A
- Banerjee, D. P. K., Joshi, V., Evans, A., et al. 2018, *MNRAS*, **481**, 806
- Baron, E., Ashall, C., DerKacy, J. M., et al. 2025, *ApJ*, **994**, 249
- Böker, T., Beck, T. L., Birkmann, S. M., et al. 2023, *PASP*, **135**, 038001
- Bose, S., & Kumar, B. 2014, *ApJ*, **782**, 98
- Bushouse, H., Eisenhamer, J., Dencheva, N., et al. 2025a, JWST Calibration Pipeline, v1.20.2, Zenodo, doi:[10.5281/zenodo.6984365](https://doi.org/10.5281/zenodo.6984365)
- Bushouse, H., Eisenhamer, J., Dencheva, N., et al. 2025b, JWST Calibration Pipeline, v1.19.1, Zenodo, doi:[10.5281/zenodo.16280965](https://doi.org/10.5281/zenodo.16280965)
- Chieffi, A., Domínguez, I., Höflich, P., Limongi, M., & Straniero, O. 2003, *MNRAS*, **345**, 111
- Davis, S., Hsiao, E. Y., Ashall, C., et al. 2019, *ApJ*, **887**, 4
- DerKacy, J. M., Ashall, C., Baron, E., et al. 2025, arXiv:2507.18785
- Dessart, L., & Hillier, D. J. 2005, *A&A*, **437**, 667
- Dessart, L., & Hillier, D. J. 2011, *MNRAS*, **415**, 3497
- Dwek, E. 2006, *Sci*, **313**, 178
- Dwek, E., & Scalzo, J. M. 1980, *ApJ*, **239**, 193
- Ertini, K., Regna, T. A., Ferrari, L., et al. 2025, *A&A*, **699**, A60
- Ferrari, L., Folatelli, G., Ertini, K., et al. 2025, *A&A*, **703**, A12
- Gall, C., Hjorth, J., & Andersen, A. C. 2011, *A&ARv*, **19**, 43
- Gamache, R. R., & Rothman, L. S. 1992, *JQSRT*, **48**, 519
- Gérard, J.-C., Hubert, B., Bisikalo, D. V., & Shematovich, V. I. 2000, *JGR*, **105**, 15795
- Gerardy, C. L., Fesen, R. A., Höflich, P., & Wheeler, J. C. 2000, *AJ*, **119**, 2968
- Gerardy, C. L., Fesen, R. A., Nomoto, K., et al. 2002, *PASJ*, **54**, 905
- Hoefflich, P. 1988, *PASA*, **7**, 434
- Hoefflich, P., Ashall, C., Bose, S., et al. 2021, *ApJ*, **922**, 186
- Höflich, P., Gerardy, C. L., Fesen, R. A., & Sakai, S. 2002, *ApJ*, **568**, 791
- Hoogendam, W., Auchettl, K., Tucker, M., et al. 2024, TNSAN, **103**, 1
- Hueichapán, E., Cartier, R., Prieto, J. L., et al. 2025, arXiv:2508.02656
- Höflich, P. 1988, *PASA*, **7**, 434
- Jacobson-Galán, W. V., Davis, K. W., Kilpatrick, C. D., et al. 2024, *ApJ*, **972**, 177
- Jakobsen, P., Ferruit, P., Alves de Oliveira, C., et al. 2022, *A&A*, **661**, A80
- Jerkstrand, A., Fransson, C., Maguire, K., et al. 2012, *A&A*, **546**, A28
- Khokhlov, A. M., Höflich, P. A., Oran, E. S., et al. 1999, *ApJL*, **524**, L107
- Kirshner, R. P., & Kwan, J. 1974, *ApJ*, **193**, 27
- Kotak, R., Meikle, P., Pozzo, M., et al. 2006, *ApJ*, **651**, L117
- Kotak, R., Meikle, P., van Dyk, S. D., Höflich, P. A., & Mattila, S. 2005, *ApJ*, **628**, L123
- Kotak, R., Meikle, W. P. S., Farrah, D., et al. 2009, *ApJ*, **704**, 306
- Law, D., Diaz, R., Sosey, M., et al. 2025, JWST Pipeline Notebooks, v1.1.0, Zenodo, doi:[10.5281/zenodo.15571377](https://doi.org/10.5281/zenodo.15571377)
- Liljegren, S., Jerkstrand, A., & Grumer, J. 2020, *A&A*, **642**, A135
- Liu, W., & Dalgarno, A. 1994, *ApJ*, **428**, 769
- Liu, W., & Dalgarno, A. 1995, *ApJ*, **454**, 472
- Liu, W., Dalgarno, A., & Lepp, S. 1992, *ApJ*, **396**, 679
- Lucy, L. B., Danziger, I. J., Gouiffes, C., & Bouchet, P. 1989, in IAU Colloq. 120: Structure and Dynamics of the Interstellar Medium, 350, ed. G. Tenorio-Tagle, M. Moles, & J. Melnick (Springer), 164
- Maeda, K., Kawabata, K., Mazzali, P. A., et al. 2008, *Sci*, **319**, 1220
- Mazzali, P. A., Kawabata, K. S., Maeda, K., et al. 2005, *Sci*, **308**, 1284
- McLeod, C., Hillier, D. J., & Dessart, L. 2024, *MNRAS*, **532**, 549
- Medler, K., Ashall, C., Hoefflich, P., et al. 2025, *ApJ*, **993**, 191
- Medler, K., Ashall, C., Shahbandeh, M., et al. 2025, *ApJS*, **281**, 28
- Meikle, W. P. S., Kotak, R., Farrah, D., et al. 2011, *ApJ*, **732**, 109
- Mera, T., et al. 2025, *ApJ*, submitted
- Modjaz, M., Kirshner, R. P., Blondin, S., Challis, P., & Matheson, T. 2008, *ApJL*, **687**, L9
- Park, S. H., Rho, J., Yoon, S.-C., et al. 2025, *A&A*, **703**, AA27
- Petuchowski, S. J., Dwek, E., Allen, J. E., Jr., & Nuth, J. A., III 1989, *ApJ*, **342**, 406
- Rho, J., Evans, A., Geballe, T. R., et al. 2021, *ApJ*, **908**, 232
- Roche, P. F., Aitken, D. K., & Smith, C. H. 1991, *MNRAS*, **252**, 39P
- Rothman, L. S., Gordon, I. E., Barber, R. J., et al. 2010, *JQSRT*, **111**, 2139
- Saha, A., Thim, F., Tammann, G. A., Reindl, B., & Sandage, A. 2006, *ApJS*, **165**, 108
- Schneider, R., Ferrara, A., & Salvaterra, R. 2004, *MNRAS*, **351**, 1379
- Shahbandeh, M., Ashall, C., Hoefflich, P., et al. 2024, arXiv:2401.14474
- Shahbandeh, M., Hsiao, E. Y., Ashall, C., et al. 2022, *ApJ*, **925**, 175
- Shahbandeh, M., Sarangi, A., Temim, T., et al. 2023, *MNRAS*, **523**, 6048
- Sharp, C. M., & Hoefflich, P. 1990, *Ap&SS*, **171**, 213
- Sharp, C. M., & Höflich, P. 1989, *HiA*, **8**, 207
- Sluder, A., Milosavljević, M., & Montgomery, M. H. 2018, *MNRAS*, **480**, 5580
- Spyromilio, J., & Leibundgut, B. 1996, *MNRAS*, **283**, L89
- Spyromilio, J., Meikle, W. P. S., Learner, R. C. M., & Allen, D. A. 1988, *Natur*, **334**, 327
- Srivastav, S., Chen, T. W., Smartt, S. J., et al. 2024, TNSAN, **100**, 1
- Stritzinger, M. D., Baron, E., Taddia, F., et al. 2024, *A&A*, **686**, A79
- Szalai, T., Vinkó, J., Balog, Z., et al. 2011, *A&A*, **527**, A61
- Takáts, K., & Vinkó, J. 2012, *MNRAS*, **419**, 2783
- Wooden, D. H., Rank, D. M., Bregman, J. D., et al. 1993, *ApJS*, **88**, 477
- Zhai, Q., Li, L., Wang, Z., Zhang, J., & Wang, X. 2024, TNSAN, **104**, 1